The Performance of Modal Filtering in Passive and Active Integrated Antenna Measurements at 160 GHz

Linus Boehm, Martin Hitzler, Alexander Foerstner, and Christian Waldschmidt
Institute of Microwave Engineering
Ulm University, Ulm, Germany
linus.boehm@uni-ulm.de

***Abstract*—The results of integrated antenna measurements are often severely distorted by reflections from the measurement environment. In order to contact and feed passive integrated antennas wafer probes have to be used. Wafer probes are not only electrically large, but are also located in the immediate environment of the antenna under test (AUT) and reflect parts of the radiated signals. This causes significant distortions and erroneous results in radiation pattern, directivity, and gain measurements. Custom wafer probes have been used to reduce reflections for meaningful measurement results, but these special probes are difficult to fabricate and expensive. If the antenna is measured within an active system that generates the transmit signal, waver probes are not required to feed the AUT, but bond wires, circuit elements close to the antenna, and surface wave radiation still limit the achievable accuracy of the measurements.**

In this paper modal filtering is used to mitigate the influence of unwanted distortions in post-processing for both wafer probe and active antenna measurements. It is shown that modal filtering can be applied to integrated antenna measurements above 100 GHz and that reflections from wafer probes, bond wires, and the PCB can be reduced significantly for passive and active antenna measurements, respectively.

I. Introduction

The accuracy of antenna measurements is limited by various error sources, like mechanical and electrical inaccuracies, reflections, probe antenna uncertainties, and processing errors [1]. While many of these error sources can be reduced with modified and optimized measurement setups, the remaining errors can still have a significant effect on the measurement result.

The first setups for 3D-measurements of integrated antennas at mm-wave frequencies used custom made rotating arms to probe the radiated field on a spherical surface [2], [3]. More recent setups were built to improve the mechanical setup for a better positional accuracy and to reduce reflections to lessen the impact of reflections in the measurement environment [4]–[6]. Measurement setups using a robotic arm to move the probe antenna around the antenna under test (AUT) offer high flexibility and accuracy for near-field measurements [7] and integrated antenna measurements [8].

Despite the improvements of integrated antenna measurement setups, the interference of the desired signal with wafer probe reflections still impede reliable results as indicated in Fig. 1. Custom probe designs (probe B Fig. 1) can be used to reduce reflections on the probe surface and to lower distortions [5], [9], but the fabrication is expensive and becomes increasingly challenging for higher frequencies. Even for active antenna measurements, where the frequencies are generated on the chip itself rather than being fed with wafer probes, bond wires, packaging, and connectors distort the radiated fields.

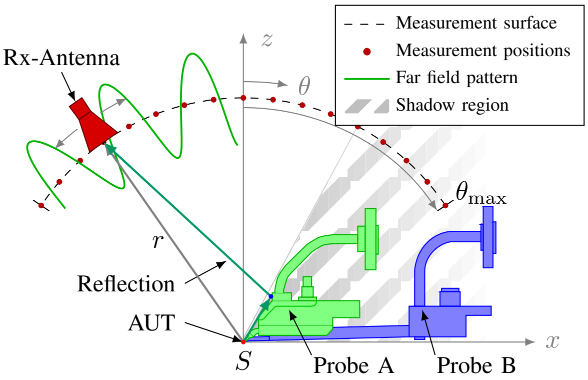

Fig. 1. Wafer probe reflections cause interference on the measurement surface. Signal blockage in the shadow region behind the probe. Measurement surface is limited by $\theta_{\max}$.

Some of these error sources cannot be mitigated by altering the setup, but the measurement results can be improved by post-processing the data. One potential approach is time-gating [10], but this requires measurement equipment and antennas with a large bandwidth to distinguish between the unwanted reflections and the direct signal, if the path difference is small.

Another way to reduce reflections in post-processing is the MARS (Mathematical Absorber Reflection Suppression) method, which was first presented in [11] for a spherical near-field range. It has since then been adjusted for other scanning geometries and to spherical far field measurements [12]. In [13] MARS is applied to integrated antenna measurements at frequencies above 100 GHz for the first time.

Section II gives a brief explanation of the MARS algorithm. A more in-depth explanation can be found in [13]. Section III shows the comparison of the post-processed measurement results of two different probes (probe A and B in Fig. 1) in order to evaluate whether post-processing makes it possible to perform reliable measurements with standard wafer probes.

Section IV shows the results of an active measurement of the same antenna and the phase retrieval method to obtain the phase of the measured signal. All measurements were performed using the robotic measurement setup described in [8].

II. MARS

The Mathematical Absorber Reflection Suppression (MARS) algorithm is a combination of modal filtering with an out-of-center antenna measurement [11].

Modal filtering is used to represent the measured far field through a set of orthogonal spherical wave functions $\mathbf{M}_{mn}^{(4)}(\mathbf{r})$ and $\mathbf{N}_{mn}^{(4)}(\mathbf{r})$ of degree n and order m for the transverse electric and the transverse magnetic field component [13]. The far field pattern of an antenna can be represented by a weighted sum of $\mathbf{M}_{mn}^{(4)}(\mathbf{r})$ and $\mathbf{N}_{mn}^{(4)}(\mathbf{r})$ [14]

$$\mathbf{E}(\mathbf{r}) = \frac{k}{\sqrt{\eta}} \sum_{n=1}^{\infty} \sum_{m=-n}^{n} \left[B_{mn}^{(1)} \mathbf{M}_{mn}^{(4)}(\mathbf{r}) + B_{mn}^{(2)} \mathbf{N}_{mn}^{(4)}(\mathbf{r}) \right] , \quad (1)$$

with $\eta = \sqrt{\varepsilon/\mu}$ and the wave number $k = 2\pi/\lambda$. The complex weighting factors $B_{mn}^{(1)}$ and $B_{mn}^{(2)}$ of the wave functions are called spherical mode coefficients (SMC) and can be calculated from a measured far field by solving (1) for $B_{mn}^{(1)}$ and $B_{mn}^{(2)}$ after splitting $\mathbf{E}(\mathbf{r})$ in an E_ϕ and an E_θ component [13], [15]. The radiated field of an antenna can therefore be fully described by the SMCs.

The function values of the spherical wave functions $\mathbf{M}_{mn}^{(4)}(\mathbf{r})$ and $\mathbf{N}_{mn}^{(4)}(\mathbf{r})$ decline strongly for $n > kr_0$, where r_0 is the minimum radius of a sphere surrounding the entire aperture of the AUT (minimum radius sphere, MRS). Thus, the number of modes required for the field representation of the AUT can be limited to

$$N = \lfloor kr_0 \rfloor + n_1 \, . \quad (2)$$

The safety margin n_1 ensures that no relevant modes are omitted.

SMCs of degree larger than N that have a significant amplitude must be caused by reflections that are outside of the MRS of the AUT. Reflections can be filtered by zeroing all modes that cannot be attributed to the AUT in (1)

$$B_{mn}^{(s)}(n > N) = 0 \, , \quad s = 1, 2 \, . \quad (3)$$

III. Passive Antenna Measurement

In order to evaluate the achievable post-processing improvement for radiation pattern and directivity measurements, an integrated antenna at 160 GHz was measured with two different wafer probes. A custom one, which is optimized for minimum reflections and a commercially available standard one. In this section n_1 was set to 10, which proved to be a good compromise between the performance of the modal filtering

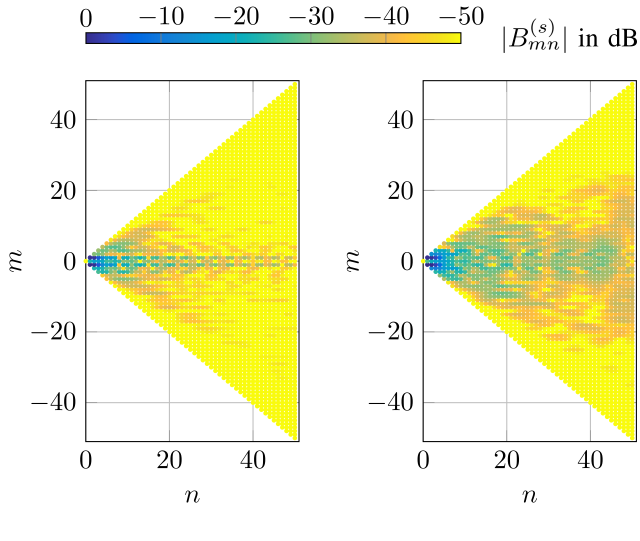

(a) $B_{mn}^{(2)}$ (b) $B_{mn}^{(2)}$

Fig. 2. Spherical mode coefficients $B_{mn}^{(2)}$ for measurement results measured with the extended wafer probe (a) and the standard wafer probe (b)

and an accurate field representation for integrated antennas with wafer probes as shown in [13]. With $kr_0 = 3.3$ the number of relevant modes to represent the isolated antenna are therefore $N = \lfloor kr_0 \rfloor + n_1 = 13$.

The number of significant modes to represent the antenna within the measurement environment is higher due to reflections in the setup. Fig. 2 shows the calculated $B_{mn}^{(2)}$ SMCs based on the measurement results using the extended probe (Fig. 2a) and the standard probe (Fig. 2b). The interference between direct radiation and reflections on the wafer probe results in an increased amplitude of higher degree modes, which are the modal equivalent to undesired ripples in the measured radiation pattern. Due to the proximity of the standard probe to the AUT, the reflections are much higher compared to the extended probe. Because of this the SMCs are spread over a larger area for standard probe measurements.

The reason for the slow decay of the weighting factors with the order $|m| = 1$ is the restricted scanning area, which was limited by $\theta_{\max} = 50°$ [13]. The mechanical setup did not allow to increase the scanning area, as the robot would have collided with the converter module, which was used to feed the AUT.

A. Radiation Pattern

The measured and simulated radiation patterns are shown in Fig. 3. The solid lines are the results after post-processing, while the dotted lines show the original data. For better comparability all measurements were normalized to the maximum value of the post-processed result of the extended probe measurement. The extended probe measurement largely agrees with the simulation result. The only significant deviations occur for θ-angles around $0°$, where reflections cause ripples on the measurement surface as shown in Fig. 3b.

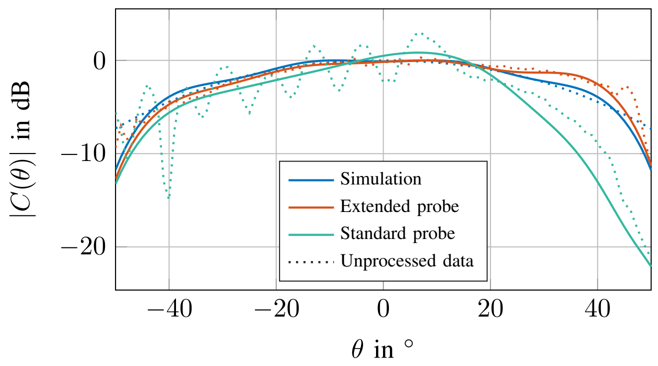

(a) E-plane ($\phi = 0°$)

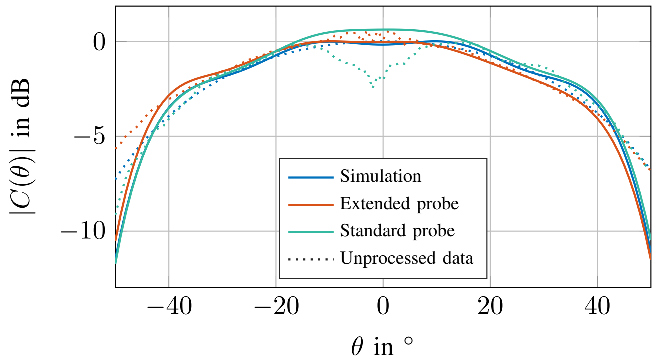

(b) H-plane ($\phi = 90°$)

Fig. 3. Comparison of measurement, simulation, and post processed radiation pattern of the integrated antenna at 160 GHz for an offset of $\Delta z = 6$ mm. The dotted lines are the unprocessed results and the solid lines the MARS post-processing results.

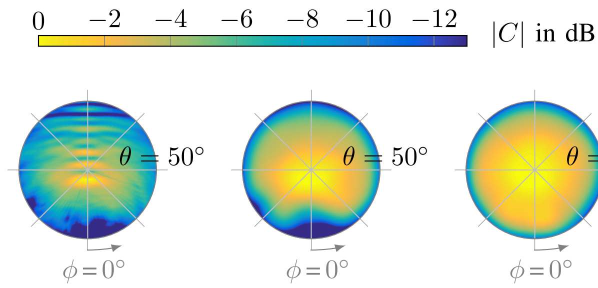

(a) Measurement with standard probe. (b) MARS with standard probe. (c) Measurement with extended probe.

Fig. 4. 3D radiation pattern of the integrated antenna at 160 GHz. The probe is located at $\phi = 0°$.

The measurements with the standard probe exhibit much stronger distortions. The H-plane measurement result shows a 2.5 dB notch around $\theta = 0°$ and large ripples with an average amplitude of approximately 3 dB occur in the E-plane. Signal blockage behind the standard probe in the E-plane causes the signal decline for $\theta > 20°$.

The largest error for the post-processed standard probe measurements occurs in the shadow region behind the probe, where the signal is blocked by the waveguide connector of the standard probe (see Fig. 1). This signal cannot be reconstructed with the MARS algorithm. Further deviations are caused by the non-physical truncation of the measured signal at the edge of the scanning surface. This results in a decrease of the post-processed radiation pattern for $\theta > 45°$, which causes the almost 5 dB difference between the dotted line (before post-processing) and the solid line (after post-processing) at the edge of Fig. 3b.

Apart form the edge and the shadow region, the difference between the two measurements and between measurement and simulation was reduced significantly from up to 5 dB before post-processing to less than 1 dB afterwards.

TABLE I
MEASURED DIRECTIVITY OF THE INTEGRATED ANTENNA AT 160 GHZ.

	Simulation	Extended probe	Standard probe
No post-processing	9.6 dB	8.7 dB	11.8 dB
MARS	9.5 dB	9.4 dB	10.7 dB

B. Directivity

The directivity was calculated by integrating over the measured radiation pattern $C(\theta, \phi)$:

$$D = \frac{4\pi}{\int_{\phi=0}^{2\pi} \int_{\theta=0}^{\pi} C^2(\theta, \phi) \sin\theta \, d\theta \, d\phi}. \tag{4}$$

As the movement of the robot is limited by the joints of the robot and by obstacles in the measurement environment, the field cannot be measured on the entire sphere. In order to determine the directivity, it was assumed that the field has the same value as on the edge of the scanning surface for angles $\theta > 50°$, i.e. $C(\theta > 50°, \phi) = C(\theta = 50°, \phi)$.

Fig. 4 shows the measured and the post-processed 3D-radiation patterns of the integrated antenna measured with the extended probe (Fig. 4c) and with the standard probe (Figs. 4a, 4b). The plots show the smoother patterns after post-processing with less reflections, the impact of the shadow region behind the standard wafer probe, and the low amplitudes at the edge of the scanning surface after post-processing due to the limited scanning surface.

The calculated directivities for simulation and measurements before and after post-processing is shown in Table I. The simulated directivity is 9.6 dB and is almost not affected by the post-processing. The difference between the extended probe measurement and the simulation was reduced from almost 1 dB to 0.1 dB.

The shadowing effect increases the measured directivity for standard probe measurements, but post-processing reduces the difference to the simulated value by approximately 1 dB.

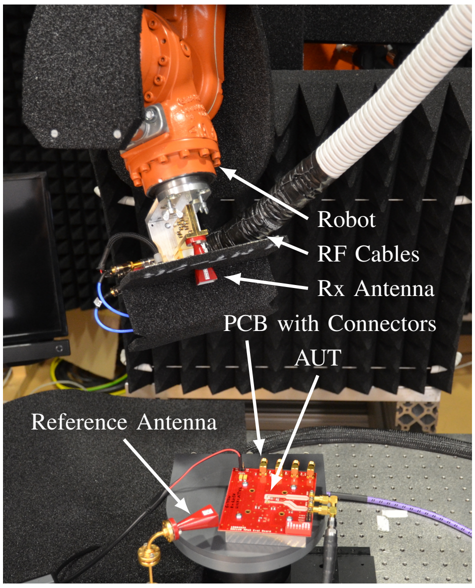

Fig. 5. Measurement setup for active measurements of an integrated antenna at 160 GHz. A static reference antenna is used to cancel out the time dependency of the phase in the measured signal.

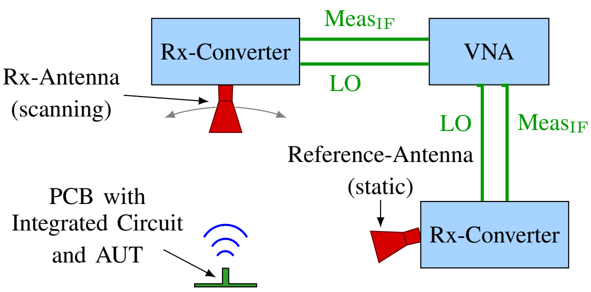

Fig. 6. Block diagram of the active antenna measurement setup. An additional reference antenna was used to measure the phase shift of the signal over time.

IV. Active Antenna Measurements

If an integrated antenna is fed by active circuitry, which is located on the same chip as the AUT, no wafer probes are required to connect the AUT with the signal generating components as shown in Fig. 5. In such a setup, however, the phase of the input signal to the AUT is not known, resulting in a time dependent phase of the measurement signal. As the phase information is required for the MARS post processing, this time dependency has to be removed such that the measured phase solely depends on the measurement location.

In this paper the phase information was obtained using a static reference antenna to measure the unwanted phase change over time as shown in Fig. 6. The time dependent phase change was then subtracted from the measurement result in post processing. This eliminated the time dependency of the phase, reducing the phase drift for a static measurement over a period of 20 minutes to less than 1°, which is a sufficient phase stability for the MARS algorithm.

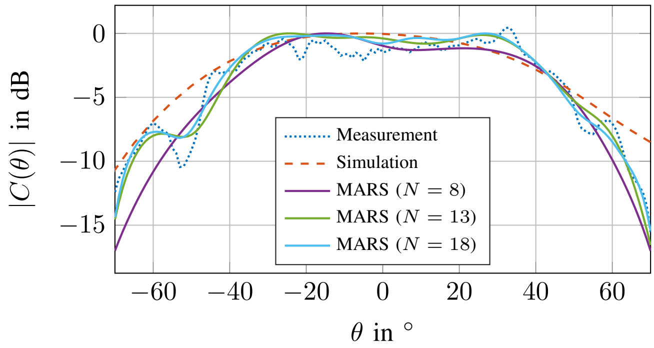

Fig. 7. Comparison of MARS result for different number of considered modes.

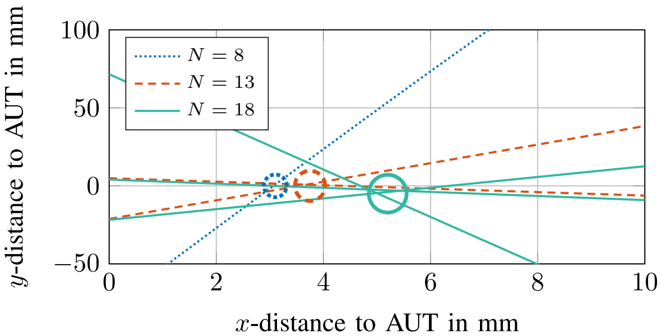

Fig. 8. Location of scattering centers for different number of considered modes N. Scattering occurs where the lines intersect with the PCB surface ($y = 0$).

A. Safety Margin n_1

[13] shows that a safety margin of $n_1 = 10$ yields the best results for measurements with wafer probes and a maximum scanning angle of $\theta = 50°$. As active measurements require no wafer probe, the scanning surface could be increased to a maximum angle of $\theta = 70°$, limited by the connectors and the reference antenna. At the same time reflections from bond wires and PCB components, like surface-mount devices and connectors, can occur closer to the AUT compared to a wafer probe measurement without PCB, where most of the reflections occur at a distance between 1 cm and 2 cm.

Fig. 7 shows a comparison of the active antenna measurement after post processing for different safety margins. It can be seen that the number of ripples increases, if a larger number of modes is used for the transformation. Based on the ripples in the pattern, the location of the scattering centers can be calculated with a quasi-optical analysis of the maxima in the far field pattern as shown in [9]. The result of this is shown in Fig. 8. As the number of considered modes is decreased, the impact of reflections is reduced. For $N = 18$, which corresponds to a MRS of 5.4 mm, the main reflections occur in a distance of around 5.1 mm. If the number of modes is reduced, these reflections can be canceled out, but undesired radiation closer to the AUT still occurs (see Fig. 8 for $N = 13$

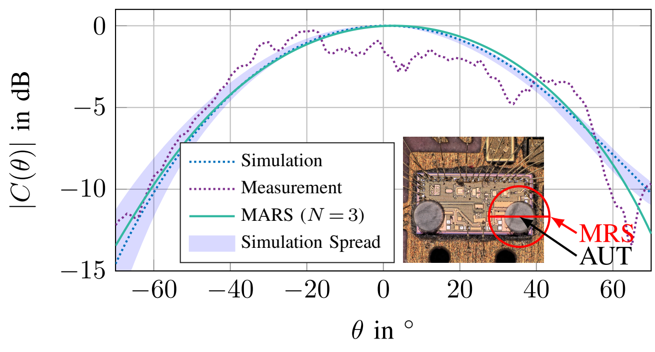

(a) E-plane

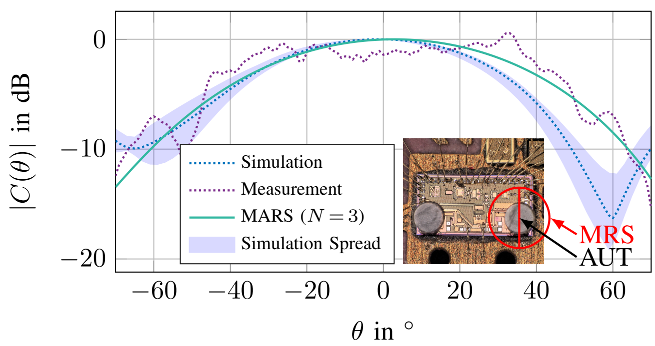

(b) H-plane

Fig. 9. Measurement, simulation, and post processed radiation patterns of the isolated chip-fed integrated antenna at 160 GHz. The highlighted area indicates the simulation results for different resonator positions (40 µm variation). The simulation model only contained the AUT. With $N = 3$, chip radiation is filtered.

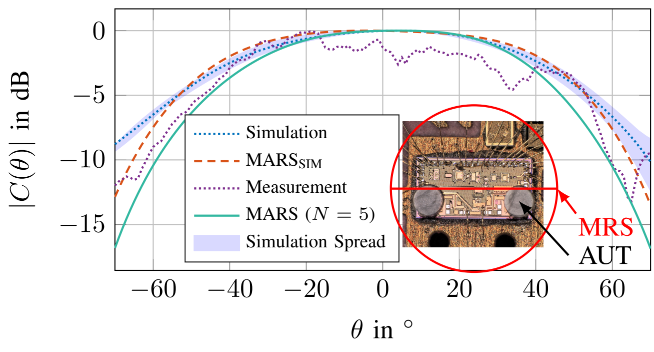

(a) E-plane

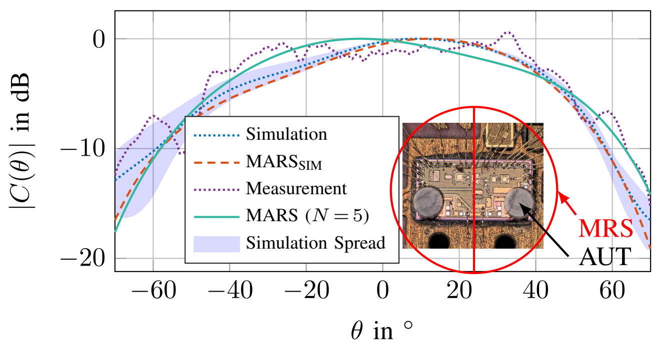

(b) H-plane

Fig. 10. Comparison of measurement, simulation, and post processed radiation patterns of the chip-fed integrated antenna at 160 GHz. $N = 5$ was chosen such that the entire chip is taken into account. The simulation model included the AUT and the chip.

and $N = 8$).

While the wafer probe measurement had no metallic objects within 5 mm of the AUT and required a safety margin of $n_1 = 10$ in order to mitigate the effect of the limited scanning surface with $\theta_{\max} = 50°$, the active measurement has different boundary conditions. In the absence of a wafer probe, the scanning area can be increased to $\theta_{\max} = 70°$ (limited by the reference antenna) and reflections can occur right next to the AUT due to the required bond wires and the printed circuit board. Therefore, the performance of the MARS algorithm can be increased with smaller values of N.

B. Radiation Pattern

Figs. 9 and 10 show the simulation and measurement results of the active measurement of the integrated antenna at 160 GHz as well as the post processed MARS result in the E- and H-plane for the safety margin $n_1 = 0$. The antenna uses a surface mounted dielectric radiator as shown in [16] to increase the radiation efficiency. As the radiator is glued manually on the chip, multiple simulations with different x- and y-offsets within 40 µm of the desired position were performed to account for possible misalignment of the real antenna. The highlighted area in Figs. 9 and 10 indicates the possible values of the radiation pattern depending on the resonator position.

In Fig. 9 only the radiation that occurs right at the antenna is taken into account ($N = 3$) and the measurement results are therefore compared to a simulation model of the isolated antenna without the rest of the chip. In both planes a significant improvement compared to the measurement result could be achieved through the MARS algorithm. In the E-plane the post-processed result closely matches the simulation with deviations well below 1 dB for all angles below 60°. The H-plane shows a bigger difference between simulation and MARS result especially for positive theta angles, which could be due to a bond wire that is right next to the AUT and within the MRS in the H-plane.

In Fig 10 the center of the MRS was moved to the center of the chip. With the given chip dimensions the number of modes has to be increased to $N = 5$, in order to take the radiation of the entire chip into account for the back transformation of the mode spectrum into the far field. The measurement is compared to a simulation of the AUT with the chip, without PCB and bond wires. As the boundary surface between filtered and unfiltered sources is spherical, the boundary cannot be traced exactly along the edges of the chip, such that some sources surrounding the chip (bond wires, capacitors) are not completely filtered out, which explains the deviations in Figs. 10a and 10b. The truncation of the signal

TABLE II
DIRECTIVITY OF THE ACTIVE INTEGRATED ANTENNA MEASUREMENT AT 160 GHZ.

Directivity	Measurement	MARS	Simulation
Isolated AUT	9.8 dB	9.1 dB	9.2 dB
Chip with AUT	9.8 dB	9.0 dB	8.7 dB

at the edge of the scanning surface also causes deviations especially for $C(|\theta| = 70) > -10\,\text{dB}$, which can be seen when comparing the simulation and the post processed simulation result (MARS_{SIM}) in Fig. 10a. Still, the influence of circuitry outside the MRS could be filtered out, resulting in a much smoother pattern of the antenna.

C. Directivity

Based on the measured far field patterns the directivity was calculated as shown in Section III-B. The results are displayed in Table II. For both measurement scenarios (isolated AUT and AUT with chip), the measured directivity can be improved through the MARS algorithm, yielding results that are within 0.3 dB of the simulation.

V. CONCLUSION

Both passive and active integrated antenna measurements suffer from unwanted reflections that distort the measurement results. For passive measurements wafer probes are the main source of reflections and active measurements are mainly influenced by surrounding circuitry like bond wires, lumped components on the PCB, and the PCB itself.

It was shown that the influence of these reflections can be reduced significantly with the MARS algorithm, improving both radiation pattern and directivity measurements. In order to optimize the results, the safety margin n_1 has to be chosen carefully. For passive measurements a larger margin of $n_1 = 10$ is favorable to mitigate the effect of a limited scanning area. As most reflections occur at a distance of more than 10 mm, the filtering effect of the MARS algorithm is barely affected by the higher margin. For active measurements reflections can occur in the immediate vicinity of the AUT. Due to bond wires and the PCB an almost gradual transition between wanted and unwanted radiation can be observed, which makes filtering the unwanted radiation more difficult. The best results were achieved for a safety margin of $n_1 = 0$, taking only sources on the structure under test (isolated antenna, antenna with chip) into account.

For passive measurements the difference between a measurement with a standard probe and an optimized probe, which was used as a reference, was reduced from 3 dB to 1.3 dB for directivity measurements and from 5 dB to 1 dB for radiation pattern measurements, apart from the shadow region behind the probe, which cannot be reconstructed. The biggest improvement for active measurements were achieved for the isolated antenna, where the post-processed measurement results were within 1 dB of the simulation, except for positive θ-angles in the H-plane. When considering the entire chip, the boundary region cannot be fitted as well around the AUT, which causes bigger deviations. The difference between the simulated and measured directivity of the active antenna was decreased from above 1 dB to 0.2 dB.

ACKNOWLEDGMENT

This work was supported by the German Research Foundation (DFG) under the project number WA 3506/1-1.

REFERENCES

[1] S. Pivnenko, J. M. Nielsen, and O. Breinbjerg, "Very High-Accuracy Calibration of Radiation Pattern and Gain of a Near-Field Probe," in *Antennas and Propagation (EuCAP), 8th European Conference on, The Hague, Netherlands*, pp. 1690–1694, IEEE, 2014.

[2] H. Gulan, S. Beer, S. Diebold, C. Rusch, A. Leuther, I. Kallfass, and T. Zwick, "Probe Based Antenna Measurements up to 325 GHz for Upcoming Millimeter-Wave Applications," *Antenna Technology (iWAT), International Workshop on*, pp. 228–231, 2013.

[3] D. Titz, F. Ferrero, and C. Luxey, "Development of a Millimeter-Wave Measurement Setup and Dedicated Techniques to Characterize the Matching and Radiation Performance of Probe-Fed Antennas [Measurements Corner]," *Antennas and Propagation Magazine, IEEE*, vol. 54, pp. 188–203, Aug. 2012.

[4] F. Ferrero, S. Gregson, J. Lanteri, L. Brochier, Y. Benoit, C. Migliaccio, and J.-Y. Dauvignac, "Spherical Near-field Probe Fed Antenna Techniques for Accurate Millimeter Wave Measurements," in *10th European Conference on Antennas and Propagation (EuCAP)*, pp. 4021–4024, Apr. 2016.

[5] A. Reniers, A. van Dommele, A. Smolders, and M. Herben, "The Influence of the Probe Connection on mm-Wave Antenna Measurements," *IEEE Transactions on Antennas and Propagation*, vol. 63, pp. 3819–3825, Sep. 2015.

[6] E. C. Lee, E. Szpindor, and W. E. McKinzie III, "Mitigating Effects of Interference in On-Chip Antenna Measurements," in *AMTA 37th Annual Meeting and Symposium, Long Beach, California, USA*, Oct. 2015.

[7] J. A. Gordon, D. R. Novotny, M. H. Francis, R. C. Wittmann, M. L. Butler, A. E. Curtin, and J. R. Guerrieri, "Millimeter-Wave Near-Field Measurements Using Coordinated Robotics," *IEEE Transactions on Antennas and Propagation*, vol. 63, no. 12, pp. 5351–5362, 2015.

[8] L. Boehm, S. Pledl, F. Boegelsack, M. Hitzler, and C. Waldschmidt, "Robotically Controlled Directivity and Gain Measurements of Integrated Antennas at 280 GHz," in *European Microwave Conference (EuMC), Paris, France*, Sep. 2015.

[9] L. Boehm, M. Hitzler, F. Roos, and C. Waldschmidt, "Probe Influence on Integrated Antenna Measurements at Frequencies Above 100 GHz," in *European Microwave Conference (EuMC), London, UK*, Oct. 2016.

[10] G. Burrell and A. Jamieson, "Antenna Radiation Pattern Measurement Using Time-to-Frequency Transformation (TFT) Techniques," *IEEE Transactions on Antennas and Propagation*, vol. 21, pp. 702–704, Sep. 1973.

[11] G. Hindman and A. Newell, "Reflection Suppression in a Large Spherical Near-Field Range," *AMTA 27th Annual Meeting & Symposium, Newport, RI*, 2005.

[12] S. F. Gregson, J. Dupuy, C. G. Parini, A. C. Newell, and G. E. Hindman, "Application of Mathematical Absorber Reflection Suppression to Far-Field Antenna Measurements," in *Loughborough Antennas Propagation Conference*, pp. 1–4, Nov. 2011.

[13] L. Boehm, A. Foerstner, M. Hitzler, and C. Waldschmidt, "Reflection Reduction through Modal Filtering for Integrated Antenna Measurements above 100 GHz," *IEEE Transactions on Antennas and Propagation*, vol. PP, pp. 3712 – 3720, Jul. 2017.

[14] C. Parini, S. Gregson, J. McCormick, and D. J. van Rensburg, *Theory and Practice of Modern Antenna Range Measurements (IET Electromagnetic Wave Series 55)*. London, United Kingdom: The Institution of Engineering and Technology, 2014.

[15] J. E. Hansen, *Spherical Near-Field Antenna Measurements (IET Electromagnetic Wave Series 26)*. London, UK: The Institution of Engineering and Technology, 2008.

[16] D. Hou, W. Hong, W.-L. Goh, J. Chen, Y.-Z. Xiong, S. Hu, and M. Madihian, "D-Band On-Chip Higher-Order-Mode Dielectric-Resonator Antennas Fed by Half-Mode Cavity in CMOS Technology," *Antennas and Propagation Magazine, IEEE*, vol. 56, pp. 80–89, Jun. 2014.